Atmos. Chem. Phys., 24, 1825–1839, 2024
https://doi.org/10.5194/acp-24-1825-2024

Atmospheric Chemistry and Physics
Open Access
EGU

Research article

Intensive photochemical oxidation in the marine atmosphere: evidence from direct radical measurements

Guoxian Zhang[1,2], Renzhi Hu[1], Pinhua Xie[1,2,3], Changjin Hu[1], Xiaoyan Liu[4], Liujun Zhong[1], Haotian Cai[1], Bo Zhu[5], Shiyong Xia[5], Xiaofeng Huang[5], Xin Li[6], and Wenqing Liu[1]

[1]Key Laboratory of Environment Optics and Technology, Anhui Institute of Optics and Fine Mechanics, HFIPS, Chinese Academy of Sciences, Hefei, China
[2]Science Island Branch of Graduate School, University of Science and Technology of China, Hefei, China
[3]College of Resources and Environment, University of Chinese Academy of Science, Beijing, China
[4]School of Pharmacy, Anhui Medical University, Hefei, China
[5]Key Laboratory for Urban Habitat Environmental Science and Technology, School of Environment and Energy, Peking University Shenzhen Graduate School, Shenzhen, China
[6]State Key Joint Laboratory of Environmental Simulation and Pollution Control, College of Environmental Sciences and Engineering, Peking University, Beijing, China

Correspondence: Renzhi Hu (rzhu@aiofm.ac.cn) and Pinhua Xie (phxie@aiofm.ac.cn)

Received: 23 March 2023 – Discussion started: 19 June 2023
Revised: 6 December 2023 – Accepted: 12 December 2023 – Published: 8 February 2024

Abstract. Comprehensive observations of hydroxyl (OH) and hydroperoxy (HO_2) radicals were conducted in October 2019 at a coastal continental site in the Pearl River Delta (YMK site, 22.55° N, 114.60° E). The daily maximum OH and HO_2 concentrations were (4.7–9.5) $\times 10^6$ and (4.2–8.1) $\times 10^8$ cm^{-3}, respectively. The synchronized air mass transport from the northern cities and the South China Sea exerted a time-varying influence on atmospheric oxidation. Under a typical ocean-atmosphere (OCM), reasonable measurement model agreement was achieved for both OH and HO_2 using a 0-D chemical box model incorporating the regional atmospheric chemistry mechanism version 2-Leuven isoprene mechanism (RACM2-LIM1), with daily averages of 4.5×10^6 and 4.9×10^8 cm^{-3}, respectively. Land mass (LAM) influence promoted more active photochemical processes, with daily averages of 7.1×10^6 and 5.2×10^8 cm^{-3} for OH and HO_2, respectively. Heterogeneous uptake had certain effects on HO_x chemistry, but the influence of the halogen mechanism was limited by NO_x level. Intensive photochemistry occurred after precursor accumulation, allowing local net ozone production comparable with surrounding suburban environments (5.52 ppb h^{-1} during the LAM period). The rapid oxidation process was accompanied by a higher diurnal nitrous acid (HONO) concentration (> 400 ppt). After a sensitivity test, HONO-related chemistry elevated the ozone production rate by 33 % and 39 % during the LAM and OCM periods, respectively. The nitric acid ($P(HNO_3)$) and sulfuric acid ($P(H_2SO_4)$) formation rates also increased simultaneously (∼ 43 % and ∼ 48 % for LAM and OCM sectors, respectively). In the ozone-prediction test, simulated O_3 decreased from ∼ 75 ppb to a global background (∼ 35 ppb) without the HONO constraint, and daytime HONO concentrations were reduced to a low level (∼ 70 ppt). For coastal cities, the particularity of the HONO chemistry tends to influence the ozone-sensitive system and eventually magnifies the background ozone. Therefore, the promotion of oxidation by elevated precursors deserves a lot of attention when aiding pollution mitigation policies.

Published by Copernicus Publications on behalf of the European Geosciences Union.

1 Introduction

The marine boundary layer (MBL) occupies 71 % of the planetary boundary layer, is a massive active carbon sink on Earth, and plays an irreplaceable role in coping with global climate change (Stone et al., 2012; Woodward-Massey et al., 2023; C. Liu et al., 2022). As a typical background atmosphere on the Earth, the MBL is equivalent to a natural smog chamber with limited anthropogenic emissions and is characterized by low NO_x (the sum of nitric oxide (NO), nitrogen dioxide (NO_2)), and nonmethane hydrocarbons (NMHCs) under a layer of clean air (Woodward-Massey et al., 2023). The lifetime of OH radical, a key oxidant, is to the order of a few hundred milliseconds (Fuchs et al., 2012). Owing to the scarcity of oxidation precursors, including nitrous acid (HONO), formaldehyde (HCHO), and NMHCs, the reaction between O^1D and water vapor generally dominates the radical initiation pathway in the marine environment. For example, in a tropical boundary layer observation experiment (reactive halogens in the marine boundary layer, RHaMBLe), ozone photolysis was found to account for 70 % of the OH radical source based on the master chemical mechanism (MCM) (Whalley et al., 2010). The vital role of ozone photolysis contrasts with typical polluted and semi-polluted areas investigated in a series of field campaigns, in which the propagation routes were found to dominate the radical source (Yang et al., 2021a; Tan et al., 2019a). Therefore, studying the radical chemistry in the MBL provides a valuable opportunity to test the current understanding of atmospheric oxidation mechanisms in a natural setting.

Since the earliest observations off the coast of northern Norfolk in the Weybourne Atmospheric Observatory Summer Experiment in June 1995 (WAOSE95), more observations and simulations of radical chemistry in the MBL environment have been conducted using ground-based, airborne, and shipborne instruments (Qi et al., 2007; Kanaya et al., 2002, 2001; Mallik et al., 2018; Woodward-Massey et al., 2023; Carpenter et al., 2011; Grenfell et al., 1999; Brauers et al., 2001; Whalley et al., 2010). Most field measurements have yielded well-reproduced OH and HO_2 concentration profiles via chemical mechanisms, with differences of within $\sim$ 20 %. However, the base model is not sufficient to describe the radical chemistry in some exceptional cases, especially with regard to the HO_2 radical. Considering the practical association between halogen (Cl, Br, and I) chemistry and heterogeneous chemistry in marine new particle formation, particularly the involvement of heterogeneous iodine-organic chemistry, exploring the synchronous influence of these mechanisms on HO_x (OH and HO_2) radical chemistry in the MBL region is a worthy endeavor (Xu et al., 2022; Huang et al., 2022). The mixing of air masses of continental and marine origin can lead to more variability in radical concentrations. During seasonal measurements of both OH and HO_2 in the Atlantic Ocean, variance analysis indicated that around 70 % of the variance of OH and HO_2 was due to diurnal behavior (in the form of photolysis frequency), whereas the remaining variance was attributed to long-term seasonal cycles (in the form of the changes in O_3, CO and air mass contribution) (Vaughan et al., 2012).

The Chinese economy has undergone rapid development in recent years, and the co-occurrence of primary and secondary regional pollution has become a severe problem (Lu et al., 2019; T. Liu et al., 2022). The interactions between air pollutants from upwind cities, shipping vessels, and other anthropogenic emissions led to precursor accumulation (Sun et al., 2020; Zeren et al., 2022). The background ozone concentration in key regions of China has increased year by year, highlighting the significant influence of anthropogenic activities on the atmospheric oxidation in background regions in China (Wang et al., 2009; Chen et al., 2022). However, little research has been dedicated to the radical chemistry and oxidation mechanism in regions with both coastal and continental features. To fill this research gap, in this study, a field campaign was conducted on photochemistry in the MBL at a coastal site in the Pearl River Delta. The OH and HO_2 radicals associated with other related species were measured in October 2019, and the radical-related oxidation process was identified to determine the photochemical efficiency in the marine atmosphere.

2 Materials and methods

2.1 Site description

As shown in Fig. 1a, this observation campaign lasted for 11 d from 18 to 28 October 2019, in Yangmeikeng (YMK, 22.55° N, 114.60° E), a coastal site in Shenzhen, Pearl River Delta. As the core city of the Greater Bay Area, Shenzhen is bordered by Dongguan to the north, Huizhou to the east, and Hong Kong to the south. The YMK site is on the Dapeng Peninsula, to the southeast of Shenzhen, between Mirs Bay and Daya Bay. As it is adjacent to the port of Hong Kong, precursors from ship emissions may influence the atmospheric chemistry. The site is a part of Shenzhen Ecological Monitoring Center station, approximately 35 m above sea level, and the sea is approximately 150 m to the east. No apparent local emissions exist, and the surrounding forest is lush (Fig. 1b). Previous literature reported the monoterpene concentration at the YMK site, with a daily mean of 0.187 ppb (Zhu et al., 2021). Abundant biogenic emissions will likely influence the local chemistry. In addition to anthropogenic and vegetation emissions, the site is also affected by the synchronization of plumes from northern cities and the South China Sea (Niu et al., 2022; Xia et al., 2021). Owing to its significant time-varying pollution characteristics, this area is an ideal site for studying the effects of plume transport on atmospheric oxidation.

Using the hybrid single-particle Lagrangian integrated trajectory (HYSPLIT) model, the 24 h backward trajectories on special days were obtained. In Fig. S1 in the Supplement,

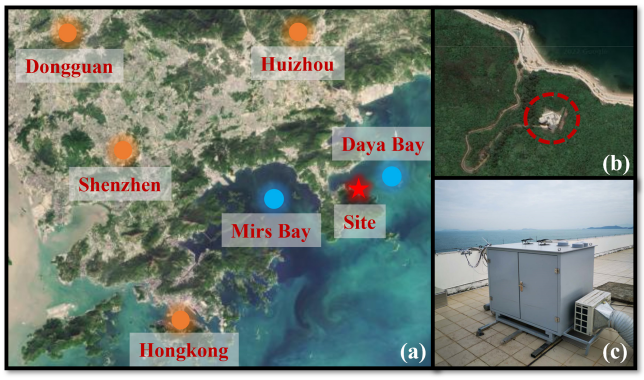

Figure 1. Details of the observation site. **(a)** The location of the measurement site and surrounding cities (source: © Google Earth). **(b)** The close shot of the measurement site location. **(c)** The actual image for the LIF Box.

the red, blue, and green trajectories represent the results at altitudes of 100, 500, and 1000 m above ground level, respectively. Two typical transportation pathways dominated the air parcels. One originated from the northern megacities in the Pearl River Delta (defined as the land mass, LAM), especially on 18, 19, and 27 October. In contrast, a clean air mass from the east or northeast was mainly transported to the observation site from the ocean (defined as the ocean mass, OCM), with representative episodes on 22, 25, and 26 October.

2.2 Instrumentation

2.2.1 HO_x radical measurements

The OH and HO_2 radicals were measured via laser-induced fluorescence (LIF). The OH radical can be directly measured by exciting the fluorescence using a 308 nm laser. HO_2 is converted into the OH radical via chemical transformation and then detected in the form of OH. The self-developed instrument, the Anhui Institute of Optics Fine Mechanics-LIF (AIOFM-LIF), was used to conduct the measurements (Zhang et al., 2022a; Wang et al., 2021, 2019). This system has been used in key regions of China, including the Yangtze River Delta, Pearl River Delta, and Chengdu-Chongqing region, and achieved good performance in a comparison experiment with a LIF system jointly developed by Forschungszentrum Jülich and Peking University (PKU-LIF) (Zhang et al., 2022b).

The system and detection interference process have been described in detail in previous studies (Zhang et al., 2022a). Briefly, the system consists of a laser output module, a radical detection module, and a control and data acquisition module. These modules are integrated into a sampling box with constant temperature and humidity control (Fig. 1c). The laser output module is a union of an Nd:yttrium-aluminum-garnet (YAG) solid-state laser, a 532 nm laser output, and a tunable dye laser. The radical detection module utilized a single-pass laser configuration, and the laser beam had a diameter of 8 mm. OH and HO_2 fluorescence cells are combined in parallel and share a common axial optical path. The 308 nm laser is introduced into the HO_2 cell first and then into the OH cell via an 8 m fiber. To maintain the detection efficiency, the power in the OH fluorescence cell should be at least 15 mW. In the detection process, a set of lenses was deployed and positioned in front of the microchannel plate detector (MCP) to boost the fluorescence collection capacity. Each MCP detector contains a timing control instrument to optimize the signal-to-noise ratio (SNR) of the fluorescence detection. Efficient ambient air sampling was achieved using an aluminum nozzle (0.4 mm orifice), and the pressure in the chamber was maintained at 400 Pa via a vortex vacuum pump (XDS35i, Edwards) to reduce fluorescence quenching.

A wavelength modulation for the background measurement that periodically switches from an on-resonant state to a nonresonant state has been widely used to obtain spectral zero. As the ozone photolysis interference is due to the laser light itself, wavelength modulation does not allow it to be removed. Through laboratory experiments, at 20 mW laser energy, every 1 % water vapor concentration and 50 ppb ozone concentration can generate a 2.5×10^5 cm^{-3} OH concentration. The results in this paper have subtracted the ozone photolysis interference (Fig. S2). In terms of system design, the AIOFM-LIF system incorporates a short-length inlet design to minimize interferences from ozonolysis and other unknown factors (the distance from radical sampling to fluorescence excitation is $\sim$ 150 mm). An OH measurement comparison with an interference-free instrument, PKU-LIF, was conducted in a real atmosphere in a previous study (Zhang et al., 2022b). The ozonolysis interference on the measurement consistency of both systems was excluded under high-volatile organic compound (VOC) conditions. Overall, the key parameters related to ozonolysis reactions (O_3, alkenes, isoprene, and NO_x) in YMK were similar to those during the intercomparison experiment, implying that the chemical conditions do not favor the generation of potential interference with OH measurement (Table S1). For HO_2 measurement, the NO gas (2 % in N_2) was utilized to achieve HO_2-to-OH conversion. NO was passed through a ferrous sulfate filter to remove impurities (NO_2, HONO, and so on) before being injected into the detection cell. The NO concentration ($\sim 1.6 \times 10^{12}$ cm^{-3}) corresponding to a conversion efficiency of $\sim$ 15 % was selected to avoid $RO_2 \rightarrow HO_2$ interference (especially from RO_2 radicals derived from long-chain alkanes ($C \geq 3$), alkenes, and aromatic hydrocarbons). A previous study noted that the percentage interference from alkene-derived RO_2 under these operating conditions was no more than 5 % (Wang et al., 2021).

A standard HO_x radical source was used to complete the calibration of the detection sensitivity (Wang et al., 2020). The radical source is based on the simultaneous photolysis of H_2O / O_2 by a 185 nm mercury lamp. Humidified air

flow is introduced to produce equal amounts of OH and HO_2 radicals after passing the photolysis region. The flow remained in a laminar condition with a maximum flow rate of 20 SLM (standard liters per minute). As the luminous flux in the photolysis region is difficult to measure accurately, the linear correlation between the ozone concentration and the 185 nm light flux was established. Ozone concentration in the flow tube was measured by a home-made Cavity Ring Down Spectrometer (CRDS, and the detection limit was 15 ppt@30 s, 1σ). The mercury lamp intensity was fine-tuned to establish a correlation between light intensity and ozone concentration. The instrument was calibrated every 1 or 2 d (except for shutdown during rainy periods), and the sensitivity used for the data processing was an average of all of the calibration results. In the YMK campaign, the relative humidity varied between 40 % and 80 % (Fig. S3). In order to test different atmospheric conditions, both low ($\sim$ 40 %) and high ($\sim$ 70 %) levels of water vapor were selected to produce OH and HO_2 radicals for calibration, and the corresponding HO_x concentration obtained from the standard source was 1.0×10^9 and 1.8×10^9 cm^{-3}, respectively (Zhang et al., 2022b).

Considering the system uncertainty and calibration uncertainty, the detection limits of the OH and HO_2 radicals were 3.3×10^5 and 1.1×10^6 cm^{-3} (60 s, 1σ), respectively. At a typical laser power of 15 mW, the measurement accuracy for OH and HO_2 measurement was 13 % and 17 % (1σ), respectively.

2.2.2 Supporting measurements

In addition to measuring the HO_x radicals, an extensive suite of relevant species was also measured close to the LIF instrument to improve the analysis of the radical photochemistry. Detailed information about the measurement instrument is presented in Table S2, including the meteorological parameters (wind speed (WS), wind direction (WD), temperature (T), relative humidity (RH), pressure (P), and solar radiation (J-values)) and chemical parameters (ozone (O_3), carbon monoxide (CO), sulfur dioxide (SO_2), HONO, NO, NO_2, HCHO, NMHCs, and particulate matter ($PM_{2.5}$)). HONO measurement was conducted using a commercial Long-Path Absorption Photometer (LOPAP). The LOPAP method utilizes two absorption tubes in series for differential correction, which effectively eliminates the influence of known interfering substances such as NO_2 and N_2O_5, offering an advantage over traditional wet chemistry methods. Zero air measurements were taken every 8 h for a duration of 20 min to correct for instrument baseline fluctuations. This method has been extensively tested for its suitability in detecting HONO in complex atmospheric conditions, as demonstrated in previous studies by Yang et al. (2022, 2021b) and Wang et al. (2023). Eight measured photolysis rates ($j(NO_2)$, $j(H_2O_2)$, j(HCHO), j(HONO), $j(NO_2)$, $j(NO_3)$, and $j(O^1D)$) were used as model constraints. In addition to HCHO, other VOCs were detected using a gas chromatograph coupled with a flame ionization detector and mass spectrometer (GC-FID-MS). Ninety-nine types of VOCs, including C_2–C_{11} alkanes, C_2–C_6 alkenes, C_6–C_{10} aromatics, halohydrocarbons, and some oxygenated VOCs (OVOCs), were observed using the GC-FID-MS at a 1 h time interval. Only isoprene was considered to be a representative of biogenic VOCs (BVOCs). All of the instruments were located close to the roof of the monitoring building, nearly 12 m above the ground, to ensure that all of the pollutants were located in a homogeneous air mass.

2.3 Model description

A 0-D chemical box model incorporating a condensed mechanism, the regional atmospheric chemistry mechanism version 2-Leuven isoprene mechanism (RACM2-LIM1), was used to simulate the radical concentrations and the generation of ozone (Stockwell et al., 1997; Griffith et al., 2013; Tan et al., 2017). The meteorological parameters, pollutants, and precursor concentrations mentioned in Sect. 2.2.2 were input into the model as boundary conditions. All of the constraints were unified to a temporal resolution of 15 min through averaging or linear interpolation. The overall average during the observations was substituted for large areas of missing data owing to instrument maintenance or failure. 3 d of data were entered in advance as the spin-up period, and a synchronized time-dependent dataset was eventually generated. The hydrogen (H_2) and methane (CH_4) concentrations were set to fixed values of 550 and 1900 ppb, respectively. The physical losses of species due to processes such as deposition, convection, and advection were approximately replaced by an 18 h atmospheric lifetime, corresponding to first-order loss rate of ~ 1.5 cm s^{-1} (by assuming a boundary layer height of about 1 km). The sensitivity analysis shows that when the lifetime changes within 8–24 h, the values differed less than 5 % for OH, HO_2, and k_{OH} (Fig. S4). According to the measurement accuracy, the simulation accuracy of the model for the OH and HO_2 radicals was 50 % (Zhang et al., 2022a).

In addition, another steady-state calculation method (PSS) can also be used to estimate the concentrations of OH and HO_2 radicals (Eqs. 1 and 2; Woodward-Massey et al., 2023; Slater et al., 2020). As the k_{OH} and RO_2 concentrations were not obtained in this observation, simulated values are used as substitutes. Other radical and reactive intermediates are actual values that measured from the instruments in Table S2.

$$[OH]_{PSS} = \frac{j_{HONO}[HONO] + \varphi_{OH} j\left(O^1D\right)[O_3] + k_{HO_2+NO}[NO][HO_2]}{k_{OH}}, \quad (1)$$

$$[HO_2]_{PSS} = \frac{k_{CO+OH}[CO][OH] + j_{HCHO}[HCHO] + k_{RO_2+NO}[NO][RO_2]}{k_{HO_2+NO}[NO]}. \quad (2)$$

Considering the environmental characteristics of the MBL, the gas-phase mechanisms for bromine (Br) and iodine (I)

were introduced into the base model to diagnose the impacts of the reactive Br and I chemistry. The details of the mechanisms involved are listed in Tables S3 and S4. The halogen species were not available at the YMK site, so the typical levels of BrO and IO concentration at the MBL site was used as a reference value (average daytime concentration of ∼ 5 ppt) (Xia et al., 2022; Bloss et al., 2010; Whalley et al., 2010).

The heterogeneous uptake of HO_2 is considered to play an important role in the MBL region (Whalley et al., 2010; Zou et al., 2023; Woodward-Massey et al., 2023). In order to assess the impact of HO_2 uptake on HO_x radical chemistry, we incorporated the HO_2 uptake reaction into the base model (Reaction R1 and Eqs. 3–4).

$$HO_2 + \text{uptake} \rightarrow \text{products}, \quad \text{(R1)}$$

$$k_{HO_2+\text{uptake}} = \frac{\gamma \times \text{ASA} \times \nu_{HO_2}}{4}, \quad (3)$$

$$\nu_{HO_2} = \sqrt{\frac{8 \times R \times T}{0.033 \times \Pi}}. \quad (4)$$

Here, ASA represents the aerosol surface area ($\mu m^2\,cm^{-3}$), which can be estimated as 20 times the $PM_{2.5}$ concentration ($\mu g\,cm^{-3}$). ν_{HO_2} (cm^{-1}) can be calculated using Eq. (4), where T and R represent the temperature and gas constant, respectively. The heterogeneous uptake coefficient (γ) for HO_2 usually has high uncertainty, with typical values ranging from 0 to 1 (Song et al., 2021). In this study, we set γ to 0.08 to evaluate the influence of HO_2 uptake on radical concentrations.

3 Results

3.1 Meteorological and chemical parameters

Figure S3 presents the time series of the main meteorological parameters and pollutants during the observation period at the YMK site. Except for on 2 d, 26 and 28 October, the meteorological characteristics of the other days were generally stable. The daily maximum T, RH, and J-values did not vary significantly. The suitable temperature (20–30° C) and humidity (40 %–80 %) conditions promoted the stable oxidation of the diurnal photochemistry. The peak $j(O^1D)$ value was approximately $2.0 \times 10^{-5}\,s^{-1}$, exhibiting the typical characteristics of intense light radiation in fall in the Pearl River Delta region (Yang et al., 2022; Tan et al., 2022).

As typical marine air components, the concentrations of NO_x, CO, $PM_{2.5}$, and other pollutants were lower than those detected in other observation campaigns in both urban and suburban areas in the Pearl River Delta region (Tan et al., 2019b; Lu et al., 2012; Yang et al., 2022). Serval observation campaigns have discovered the relationship between wind direction and radical chemistry (Lu et al., 2012; Fuchs et al., 2017; Niu et al., 2022). Although there was no apparent wind-speed condition, the dominant air mass still influenced the pollutant concentrations owing to the particularity of the marine site.

During the OCM period, the NO_x and HCHO concentrations exhibited relatively clean characteristics that were consistent with those previous observations in the open ocean (RHaMBLe, SOS, CHABLIS, and ALBATROSS, Table 1). Isoprene, a representative BVOC, achieved a diurnal concentration of 0.58 ± 0.06 ppb, indicating that slight local emissions could have impacted the concentrations of the precursor species, even in OCM sector. The ozone concentration at the YMK site was always at the critical value of the updated Class I standard (GB3095-2012, average hourly O_3 of 81 ppb at 25° C and 1013 kPa). The occurrence of fewer emissions reduced the titration effect, resulting in the ozone exhibiting no apparent diurnal trend on some of the dates and a high background value at night (78.1 ± 7.6 ppb).

As a coastal site, chemical conditions could be influenced by local land emissions depending on the wind direction. Compared with the OCM period, the meteorological conditions (T, RH, and J-values) changed slightly during the LAM episode, but the pollutants were accumulated owing to the transport of the plume from the northern cities (Fig. 2). The CO and $PM_{2.5}$ concentrations exhibited good consistency and even mild pollution features (0.36 ± 0.12 ppm and $37.70 \pm 7.91\,\mu g\,m^{-3}$, respectively), reflecting the influence of human activities. Both NO and NO_2 peaked at around 10:00 CST, exhibiting prominent pollution characteristics. HONO exhibited a distribution with high daytime (0.66 ± 0.08 ppb) and low nighttime (0.33 ± 0.09 ppb) concentrations. This unique distribution of HONO has been observed in remote environments in several previous observation campaigns (Jiang et al., 2022; Crilley et al., 2021). High HONO concentration in the daytime affects the chemical composition of the atmosphere and the secondary pollution generation.

The detailed information for VOC species during the YMK campaign has been added in Table S5. The daily maximum NMHC concentration peaked at 27.81 ± 9.91 ppb, and the maximum value of ∼ 40 ppb occurred on 27 October. Local biological emissions significantly affected the NMHC composition of the site, and isoprene achieved a noon maximum of 0.82 ± 0.16 ppb. Neither anthropogenic alkenes (2.21 ± 0.94 ppb) nor aromatic (1.31 ± 0.25 ppb) hydrocarbons were abundant, and OVOCs accounted for approximately 50 % of the total. As a photochemical indicator, formaldehyde peaked at ∼ 4 to ∼ 8 ppb during the LAM episode, suggesting a more vigorous oxidation process. The HONO concentration was 6.8 times higher than the SW scenario in the ICOZA observation (a pollution period dominated by a southwest wind direction), whereas the HCHO concentration was 3.1 times higher (Woodward-Massey et al., 2023). The abundance of oxidation precursors (HONO, HCHO, O_3, and NMHCs) reflected the unique atmospheric conditions in the marine environment in China, which originated from the complex atmospheric pollution.

Figure 2. Mean diurnal profiles of measured trace gases parameters during Land mass and Ocean mass episodes. The colored shadows denote the 25 % and 75 % percentiles. The gray areas denote nighttime.

Table 1. Summary of radical concentrations and related species concentrations at MBL. All data are listed as the average during noontime (10:00–15:00 CST).

Campaign	Location	Category	Date	OH (10^6 cm^{-3})	HO_2 (10^8 cm^{-3})	HCHO (ppb)	HONO (ppb)	NO_x (ppb)	O_3 (ppb)	Reference
WAOSE95	Weybourne, UK	Coastal	1995 (June)	5.0	–	1.50	0.10	< 2.0	40.0	Grenfell et al. (1999)
ALBATROSS	Atlantic Ocean	Open ocean	1996 (October–November)	7.0	–	0.50	–	–	25.0	Brauers et al. (2001)
EASE96	Mace Head, Ireland	Coastal	1996 (July–August)	2.3	2.6	–	–	~ 1.0	45.0	Carslaw et al. (1999)
EASE97	Mace Head, Ireland	Coastal	1997 (April–May)	1.8	1.0	0.70	–	0.95	46.0	Creasey et al. (2002)
ORION99	Okinawa Island, Japan	Coastal	1999 (August)	4.0	4.3	–	0.20	6.3	23.0	Kanaya et al. (2001)
RISOTTO	Rishiri Island, Japan	Coastal	2000 (June)	7.4	3.1	–	–	0.45	–	Kanaya et al. (2002)
RISFEX	Rishiri Island, Japan	Coastal	2003 (August)	2.7	1.5	–	–	0.2	28.0	Qi et al. (2007)
CHABLIS	Antarctica	Open ocean	2005 (January–February)	1.0	1.1	0.12	0.007	0.02	7.0	Bloss et al. (2010)
RHaMBLe	Atlantic Ocean	Open ocean	2007 (May–June)	9.0	6.0	0.30	–	0.014	35.0	Whalley et al. (2010)
SOS	Cape Verde, Atlantic Ocean	Open ocean	2009 (June; September)	9.0	4.0	1.9	–	0.050	40.0	Carpenter et al. (2011)
CYPHEX	Cyprus, Mediterranean	Coastal	2014 (July)	5.8	6.3	~ 1.0	~ 0.080	< 1.0	69.0	Mallik et al. (2018)
ICOZA (NW-SE)	North Norfolk, UK	Coastal	2015 (July)	3.0	1.4	0.9	0.052	2.0	39.0	Woodward-Massey et al. (2023)
ICOZA (SW)	North Norfolk, UK	Coastal	2015 (July)	4.1	1.0	1.1	0.097	3.0	31.0	Woodward-Massey et al. (2023)
HT	Hok Tsui, China	Coastal	2020 (October–November)	4.9	–	1.0	0.15	~ 4.0	65.0	Zou et al. (2023)
YMK (Land Mass)	Shenzhen, China	Coastal	2019 (October)	7.1	5.2	3.4	0.66	6.4	75.6	This work
YMK (Ocean Mass)	Shenzhen, China	Coastal	2019 (October)	4.5	4.9	1.2	0.48	3.0	78.1	This work

3.2 HO_x radical concentrations and modeled OH reactivity

Figure 3a, b shows the time series of the simulated and observed OH and HO_2 radical concentrations during the observation campaign. The time series of the simulated OH reactivity (k_{OH}) is presented in Fig. 3c. The observed OH and HO_2 radicals exhibited significant diurnal trends. The daily maximum OH and HO_2 values were (4.7–9.5) $\times 10^6$ and (4.2–8.1) $\times 10^8$ cm^{-3}, respectively. The peak k_{OH} value was commonly less than 10 s^{-1}. Owing to human activities, the simulated k_{OH} reached more than ~ 15 s^{-1} on some days. The radical concentrations and reactivity exhibited similar trends, which differed from reports on urban and semi-urban areas where inorganic species (NO_x and CO) were the dominant controllers of k_{OH} (Zhang et al., 2022a; Tan et al., 2019b; Lou et al., 2010). The k_{OVOCs} was separated into $k_{OVOCs(Obs)}$ and $k_{OVOCs(Model)}$ (Fig. 3c). Specifically, $k_{OVOCs(Obs)}$ includes the observed species such as

formaldehyde (HCHO), acetaldehyde (ACD), higher aldehydes (ALD), acetone (ACT), ketones (KET), and oxidation products of isoprene (MACR and MVK). The model-generated intermediates, such as glyoxal, methylglyoxal, methylethyl ketone, and methanol, are categorized as $k_{\mathrm{OVOCs(Model)}}$. Approximately 50 % of the total k_{OVOCs} are represented by unconstrained species ($k_{\mathrm{OVOCs(Model)}}$), which contribute a daily k_{OH} of $1.39\,\mathrm{s}^{-1}$. Overall, the observed OH and HO_2 concentrations were both well reproduced by the base model incorporating the RACM2-LIM1 mechanism. The observed OH was underestimated only on the first days, and a slight model overestimation happened on 23 and 24 October. PSS calculation showed good agreement with the base model, providing evidence of the balance of radical internal consistency in the daytime. It should be noted that the OH reactivity of unmeasured VOCs may be underestimated owing to the lumped groups in the RACM2 mechanism.

The air mass transport of the precursors induced photochemistry accumulation, which was then reflected in the changes in the oxidation progress. It is worth comparing the concentrations and reactivities of the radicals by classifying the predominant air mass (Fig. 4). During the OCM period, the observed OH and HO_2 radicals could be reflected by the base chemical mechanism, with daily averages of 4.5×10^6 and $4.9 \times 10^8\,\mathrm{cm}^{-3}$, respectively. Compared with other campaigns (Table 1), the observed maximum values were within reasonable ranges (OH: 2–$9 \times 10^6\,\mathrm{cm}^{-3}$; HO_2: 1–$6 \times 10^8\,\mathrm{cm}^{-3}$). Despite low NO_x levels during the OCM period, the HO_2 radical was not overestimated using the base model, which was dissimilar to many MBL observations (Bloss et al., 2010). However, both the OH and HO_2 radical concentrations reached higher levels during the LAM-dominant period, indicating a more active photochemical process (Sect. 4.1). The diel averages for the OH and HO_2 radicals were 7.1×10^6 and $5.2 \times 10^8\,\mathrm{cm}^{-3}$, respectively, which were notably higher than the levels reported in the ICOZA observations (Woodward-Massey et al., 2023). The base scenario underestimated both the OH and HO_2 concentrations between 10:00 and 15:00 CST, and the observation-to-model ratio was greater than 1.2. The calculated daily maximum total OH reactivity was $8.8\,\mathrm{s}^{-1}$, and nearly 70 % of the reactivity was accounted for by the organic species, among which the OVOCs were the largest contributor (30.6 %). The anthropogenic alkanes, alkenes, and aromatic hydrocarbons contributed less than 10 % to the reactivity. Compared with the OCM-dominant episode, the higher reactivity during the LAM period indicated the occurrence of efficient recycling during the RO_x (the sum of OH, HO_2, and RO_2) propagation ($12.4\,\mathrm{s}^{-1}$ vs. $8.8\,\mathrm{s}^{-1}$). The higher contributions of the BVOCs (only isoprene was considered, 15.6 %) and OVOCs (30.2 %) to the reactivity reflected the diverse composition of the VOCs in the forest environment. Under enhanced photochemistry, the calculated OH reactivity could be an underestimation of the total OH reactivity, so a missing OH source may be masked. As a representative of the OVOCs, HCHO reflects the photochemical level to a certain extent. As shown in Fig. S5, a solid positive dependence between the OH_{obs}-to-OH_{mod} ratio and HCHO was observed (the daytime data were restricted according to $j(O^1D) > 5 \times 10^{-6}\,\mathrm{s}^{-1}$). With the increase in photochemical intensity, the ratio between the observed and simulated OH radical showed an obvious mismatch. Obtaining the full magnitude of the radical-related parameters is necessary to compensate for the discrepancy in the concentration closure experiments.

Halogen species have been recognized as potent oxidizers that can boost photochemistry (Xia et al., 2022; Peng et al., 2021). A sensitivity test was performed by imposing BrO and IO on the base model to diagnose the impact of the halogen chemistry on the troposphere chemistry. The concentration of BrO and IO is set to ∼ 5 ppt, which is a typical level at the MBL site (Xia et al., 2022; Bloss et al., 2010; Whalley et al., 2010). The details of the mechanisms involved are listed in Tables S3 and S4. In this scenario (Fig. 4, green line), the daytime concentration of HO_2 radical decreased by 8.5 % and 13.3 % during the LAM and OCM periods, respectively, compared with the base model. However, there was no significant change in the concentration of OH radicals (< 3 %). Traditionally, it is believed that the inclusion of halogen chemistry leads to higher modeled OH concentrations and lower modeled HO_2 concentrations. Therefore, the lack of an increase in OH concentration with the introduction of the halogen mechanism at the YMK site calls for further investigation (Fig. S6). By modifying the NO concentration in different levels (Scenario 1: [NO] × 150 %, Scenario 2: base, Scenario 3: [NO] × 20 %, Scenario 4: [NO] × 10 %), the response of HO_x radicals to the halogen mechanism varied under different NO levels. As the constrained NO increased from 30 to 500 ppt, the reduction in HO_2 radicals due to the Br and I mechanisms ranged between 10 % and 20 %. At elevated NO_x levels, reactions between halogen radicals and NO_x occurred, inhibiting the formation of OH radicals. In Scenario 1, the OH concentration even decreased by 3.5 % when introducing the halogen mechanism. When NO concentration was constrained around 30 ppt (Scenario 4), similar to those obtained in RHaMBLe and CYPHEX campaigns, the modeled OH concentration increased by 14.4 %, whereas the HO_2 concentration decreased by approximately 20.8 % (Whalley et al., 2010; Bloss et al., 2010). Therefore, the sensitivity of OH radicals to the halogen mechanism in the YMK region is primarily limited by the local NO_x concentration level.

Although the modeled and measured HO_2 showed good agreement, the effect of HO_2 heterogeneous processes on the chemistry of HO_x radicals is also worth exploring. The inclusion of heterogeneous processes ($\gamma = 0.08$) did reduce the modeled HO_2 concentration for ∼ 10 % during both LAM and OCM periods (Fig. 4, yellow line). This reduced agree-

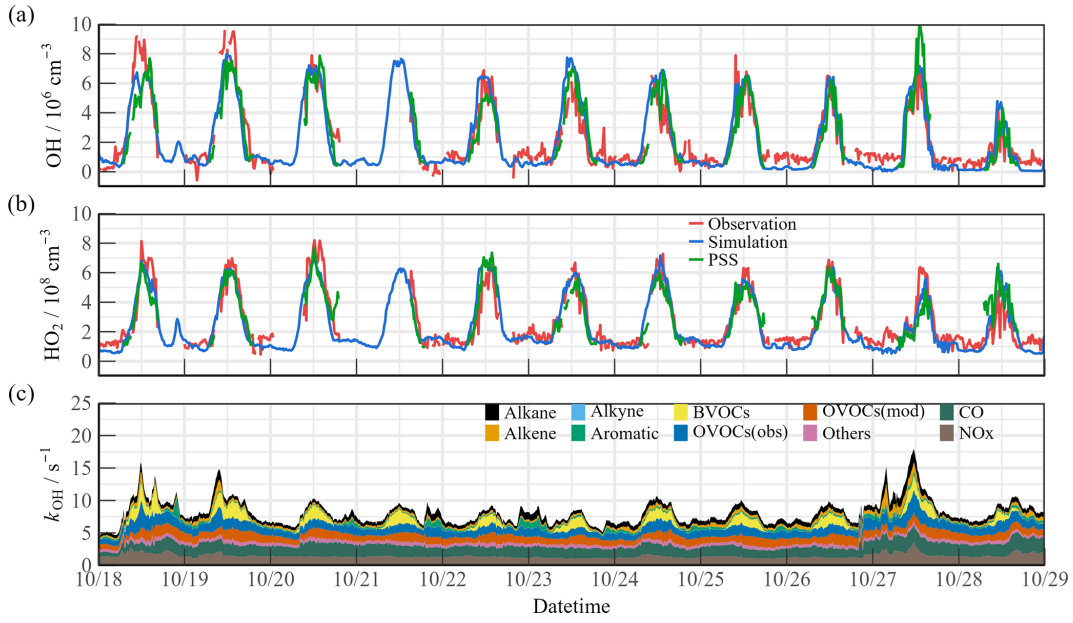

Figure 3. Timeseries of the observed and modeled parameters for OH, HO_2, and k_{OH} during the observation period. **(a)** OH, **(b)** HO_2, **(c)** k_{OH}.

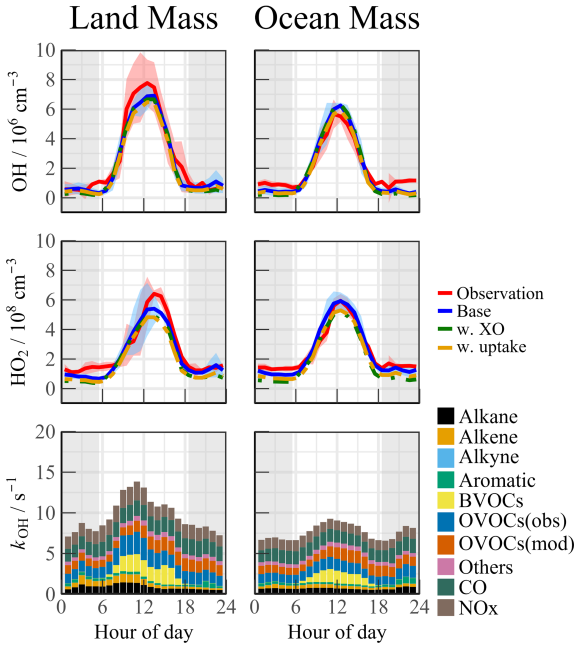

Figure 4. Median diurnal profiles of the observed and modeled OH, HO_2, and k_{OH} during LAM and OCM episodes. The colored shadows for OH and HO_2 radicals denote the 25 % and 75 % percentiles. The gray areas denote nighttime.

ment between observation and simulation emphasizes the presence of a missing HO_2 source in the base model.

4 Discussion

4.1 Experimental radical budget balance

4.1.1 OH radical

A process-oriented experiment was conducted to investigate the photochemistry progress from a budget balance perspective (Woodward-Massey et al., 2023; Tan et al., 2019b; Yang et al., 2021a). The OH was in a photostationary steady state owing to its short lifetime. The total OH removal rate was directly quantified from the union of the OH concentration and the reactivity (Eq. 5):

$$D(\mathrm{OH}) = [\mathrm{OH}] \times k_{\mathrm{OH}}. \quad (5)$$

The total production rate of the OH radical was the sum of the primary sources (O_3 / HONO photolysis and ozonolysis reactions) and secondary sources ($HO_2 + NO$) (Eq. 6):

$$\begin{aligned} P(\mathrm{OH}) = {} & j_{\mathrm{HONO}}[\mathrm{HONO}] + \varphi_{\mathrm{OH}} j\left(\mathrm{O^1D}\right)[\mathrm{O_3}] \\ & + \Sigma i\left\{\varphi^i_{\mathrm{OH}} k^i_{\mathrm{Alkenes+O_3}}[\mathrm{Alkenes}][\mathrm{O_3}]\right\} \\ & + \left(k_{\mathrm{HO_2+NO}}[\mathrm{NO}] + k_{\mathrm{HO_2+O_3}}[\mathrm{O_3}]\right)[\mathrm{HO_2}]. \end{aligned} \quad (6)$$

Here, φ_{OH} and φ^i_{OH} represent the OH yields in the O_3 photolysis and alkene ozonolysis processes, respectively.

The diel profiles of the experimental OH budget during the LAM and OCM periods are shown in Fig. 5. Both the observed OH and HO_2 radicals were introduced into the budget calculations. Because k_{OH} was not measured during the observation experiment, the simulated value was used to an-

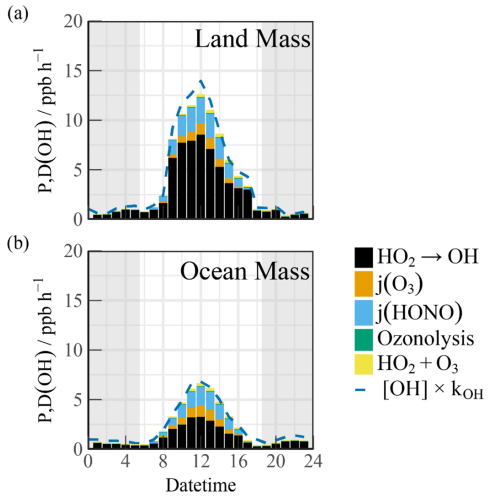

Figure 5. The diurnal profiles of the experimental OH budget during **(a)** LAM and **(b)** OCM episodes. The blue line denotes the OH destruction rate ([OH] × k_{OH}). The gray areas denote nighttime.

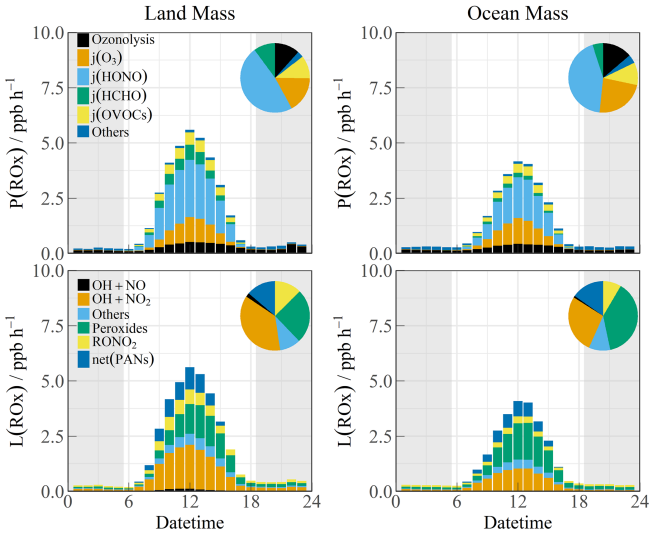

Figure 6. The diurnal profiles of RO_x budget during Land mass and Ocean mass episodes. The pie chart denotes proportions in different parts during the daytime (10:00–15:00 CST). The gray areas denote nighttime.

alyze the removal rate. Therefore, D(OH) should be considered a lower limit as it uses calculated rather than measured k_{OH} (Yang et al., 2022). During the OCM period, the $HO_2 + NO$ reaction accounted for ∼ 50 % of the OH yield. The maximum of 6.6 ppb h^{-1} occurred at around 12:00 CST. The photolysis reactions could increase the daytime contributions of HONO and O_3 to 1.52 and 0.84 ppb h^{-1}, respectively (10:00–15:00 CST). The contribution of the nonphotolytic radical source (ozonolysis reactions) was almost negligible.

Compared with other marine observations, the calculated OH generation rate was approximately twice that reported in the ICOZA and five times that obtained in the RHaMBLe campaigns (Woodward-Massey et al., 2023; Whalley et al., 2010). During the LAM period, the OH generation rate reached a maximum of 12.6 ppb h^{-1}, accompanied by a secondary source contribution of 67 % (from the reaction between HO_2 and NO) during the daytime, which was close to several observations related to polluted plumes (Woodward-Massey et al., 2023; Tan et al., 2019b; Lu et al., 2012; Yang et al., 2022). When the simulated k_{OH} was introduced into the experimental budgets, the difference between P(OH) and D(OH) was less than 2 ppb h^{-1}.

4.1.2 Total RO_x radicals

The budget analysis of the HO_2 and RO_2 radicals could not be performed well owing to the lack of RO_2 radical observation data. The diurnal profiles of the RO_x production ($P(RO_x)$) and termination rate ($L(RO_x)$) for the different air masses are shown in Fig. 6. The $P(RO_x)$ could reach 3.36 ppb h^{-1} with an ocean plume. HONO photolysis controlled nearly half of the primary sources (45.7 %), and the daily distribution was consistent with that of solar radiation. The ozone-related contributions from photolysis and ozonolysis were approximately 46.6 % (25.1 % from photolysis and 11.5 % from ozonolysis, respectively). The remaining contribution was from the photolysis of carbonyls (HCHO and OVOCs) (15.0 %). The anthropogenic contribution to the radical chemistry could not be ignored, and the RO_x source in this observation was exponentially higher than that in other MBL observations (Woodward-Massey et al., 2023; Stone et al., 2012; Whalley et al., 2010; Mallik et al., 2018). The $P(RO_x)$ of the LAM was close to that in Shenzhen (∼ 4 ppb h^{-1}) but was significantly lower than that in Yufa (∼ 7 ppb h^{-1}) and the BackGarden (∼ 11 ppb h^{-1}) (Tan et al., 2019b; Lu et al., 2012; Yang et al., 2022). The reactions between RO_x and NO_x and self-combination were the main pathways of radical termination (∼ 70 %). The contribution of the formation of peroxynitrate to the $L(RO_x)$ could not be ignored in the daytime.

The high daytime HONO concentrations observed at the YMK site constitute a notable phenomenon. Owing to the high HONO concentration during the daytime, the photolysis reaction made daytime contributions of 1.52 and 2.19 ppb h^{-1} during the OCM and LAM periods, respectively. As the only known gas-phase source, OH + NO accounted for a negligible proportion of the HONO production rate. Given the location of the site, HONO from cruiseship emissions is a possible component of the primary anthropogenic source (Sun et al., 2020). Other active tropospheric HONO sources (heterogeneous reactions with NO_2 and $p(NO_3^-)$ photolysis) are worthy of consideration and contribute significantly to the atmospheric oxidation in the MBL area (Zhu et al., 2022; Crilley et al., 2021).

4.2 Local ozone production rate

Peroxy radical chemistry is the essential photochemical source of tropospheric ozone ($F(O_x)$, Eq. 7):

$$F(O_x) = k_{HO_2+NO}[NO][HO_2] + \sum_i (1-\alpha_i) k_{RO_2^i+NO}[NO]RO_2^i. \quad (7)$$

NO reacts with HO_2 and RO_2 radicals to form NO_2, and then photolysis occurs to form O_3 under solar radiation. NO_2 and ozone are the two sides of the oxidation reservoir. The effect of local emissions on the photodynamic equilibrium can be avoided by characterizing the photochemical production of the total oxidants (Tan et al., 2019b). α_i represents the organic nitrate yield, which affects the amount of NO_2 that is produced from the reaction between RO_2 and NO (Tan et al., 2018b). O_x is mainly photochemically removed through ozone photolysis, ozonolysis, radical chain propagation ($OH / HO_2 + O_3$), and chain termination ($OH + NO_2$) reactions in the troposphere ($D(O_x)$, Eq. 8):

$$D(O_x) = \varphi_{OH} j\left(O^1D\right)[O_3] + \Sigma i\left\{k^i_{Alkenes+O_3}[Alkenes][O_3]\right\} + \left(k_{O_3+OH}[OH] + k_{O_3+HO_2}[HO_2]\right)[O_3] + k_{OH+NO_2}[OH][NO_2]. \quad (8)$$

The net formation rate $P(O_x)$ can be calculated by subtracting $D(O_x)$ from $F(O_x)$ (Eq. 9):

$$P(O_x) = F(O_x) - D(O_x). \quad (9)$$

The simulated RO_2 radical concentration was introduced into the $F(O_x)$ calculation. The diurnal variations in the ozone generation in the different air masses are shown in Fig. 7. The contribution of the HO_2 radical to $F(O_x)$ was approximately 60 %. The RO_2 radicals consisted of various types such as methyl peroxy (MO_2), acetyl peroxy radicals (ACO_3 / RCO_3), and other radicals derived from alkanes (ALKAP), alkenes (ALKEP), and isoprene (ISOP), which accounted for an additional 40 % of the $F(O_x)$. On a daytime basis, the maximum $F(O_x)$ reached 7.4 ppb h^{-1} at around 12:00 CST in the OCM period, whereas a persistently high value (maximum of 12.5 ppb h^{-1} between 10:00 and 14:00 CST) occurred during the LAM period. A vast amount of O_x was consumed in the nitric acid ($OH + NO_2$) formation pathways, i.e., higher than the ozonolysis removal. The daily averaged ozone production rates were 5.52 and 2.76 ppb h^{-1} during the LAM and OCM periods, respectively.

4.3 Relationship between precursors and oxidation rates

Despite the low level of human activities, oxidation precursors have an extended lifetime in the stable atmosphere of coastal areas. Intensive photochemical reactions occur after the accumulation of precursors, resulting in local net ozone production comparable with that in the surrounding suburban environments (Zeren et al., 2022). Simultaneous observations of both urban and coastal settings in Shenzhen have indicated that the oxidation rates are comparable (Xia et al., 2021). The coupling of precursor transport and local photochemical processes in marine areas makes it meaningful to explore secondary pollution generation (Fig. 8a, b, and c). No obvious radical source was missing during the LAM and OCM periods, and the oxidation level was that expected from the base model. On a daytime basis, the mean diurnal profile of the $P(O_x)$ reached ~7 ppb h^{-1} during the LAM period, and the average nitric acid ($P(HNO_3)$) and sulfuric acid ($P(H_2SO_4)$) production rates were ~1.6 and ~0.11 ppb h^{-1}, respectively. The $P(HNO_3)$ production rate was similar to the average of observations in the Pearl River Delta region (~1.3 ppb h^{-1}), whereas that of the $P(H_2SO_4)$ was only half the average level (~0.24 ppb h^{-1}) (Lu et al., 2013; Tan et al., 2019b; Yang et al., 2022). During the OCM period, the characteristics of the ocean air mass alleviated the photochemical process, and the production rates of the secondary pollutants decreased by approximately half and were close to the average levels in winter (Ma et al., 2019).

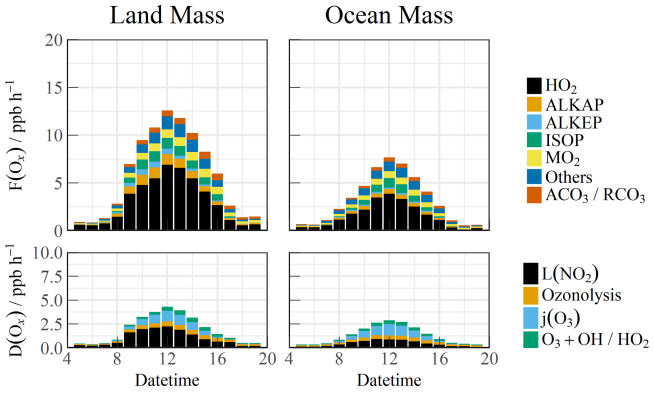

Figure 7. The diurnal profiles of the speciation $F(O_x)$ and $D(O_x)$ during Land mass and Ocean mass episodes. The data were calculated by the measured OH and HO_2 and modeled RO_2 radicals.

Contrary to numerous ocean observations, at the YMK site, intensive oxidation was accompanied by a high diurnal HONO level (higher than 400 ppt) (Fig. 9). The ozone levels were consistent with the Grade I air quality standard and far exceeded the global background concentration (~40 ppb). Daytime photolysis reactions of HONO contributed 1.52 and 2.19 ppb h^{-1} to $P(RO_x)$ during the OCM and LAM periods, respectively, which were much higher than the values in several megacities during the photochemically polluted season (Tan et al., 2019a). Given the significance of HONO photolysis in driving atmospheric chemistry, a sensitivity test was conducted without constraints on HONO (i.e., w.o HONO) to specifically quantify the contribution of HONO-

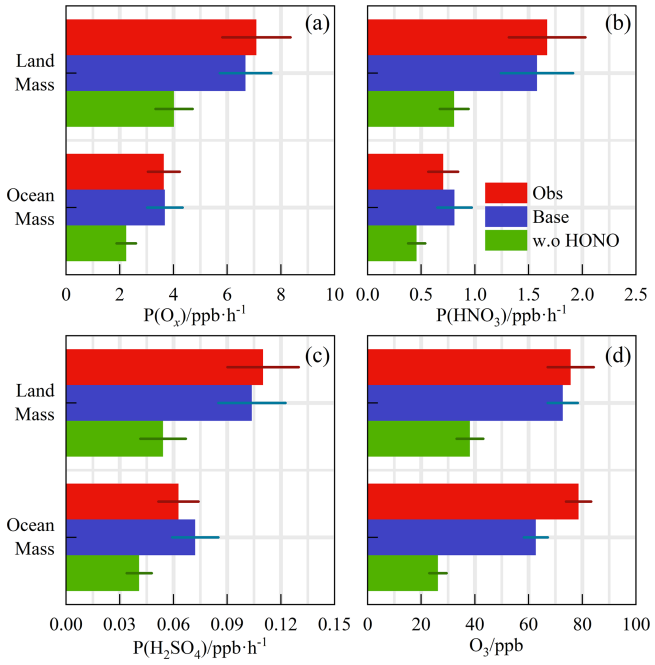

Figure 8. The calculated reaction rates based on the observed concentrations for Land mass and Ocean mass episodes **(a)** $P(O_x)$, **(b)** $P(HNO_3)$, and **(c)** $P(H_2SO_4)$. **(d)** The observed and modeled O_3 concentration with a first-order loss term. The deposition or mixing processes were equivalent to a lifetime of 18 h to all species. All the rates and concentrations are averaged for the daytime period between 10:00 and 15:00 CST.

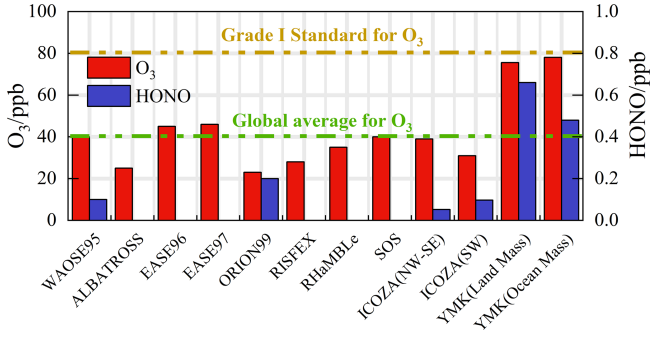

Figure 9. Summary of both ozone and HONO concentrations in previous marine observations. The concentrations are averaged for the daytime period between 10:00 and 15:00 CST.

induced secondary pollution. Only the homogeneous reaction (OH + NO) participated in the formation of HONO in the default mode without HONO input (Liu et al., 2022).

The modeled OH, HO_2, and RO_2 change when the model was unconstrained to HONO were shown in Fig. S7. After evaluation, in LAM and OCM sectors, concentration changes for OH were 46.9 % and 43.2 %, for HO_2 38.3 % and 34.3 %, and for RO_2 43.7 % and 39.0 %, respectively. The $P(O_x)$ was found to be 33 % and 39 % lower during the LAM and OCM periods, respectively. The nitric acid ($P(HNO_3)$) and sulfuric acid ($P(H_2SO_4)$) formation rates also increased simultaneously (~ 43 % and ~ 48 % for the LAM and OCM sectors, respectively). The sensitivity test identified the privileged role of the HONO-related mechanisms in the OH chemistry, which resulted in a correlation between the efficient radical recycling and secondary pollution.

A time-dependent box model was used to test the association between the HONO chemistry and the local ozone generation (Fig. 8d). The loss of model-generated O_3 by deposition or mixing was represented as a first-order deposition rate corresponding to a lifetime of 18 h. Comparatively, removing the constraints on ozone and NO while keeping NO_2 as a constraint is a commonly used method in the box model for ozone prediction (Tan et al., 2018a). Considering the complexity of HONO chemistry, we emphasize that this is a sensitivity test for ozone prediction, and its validity has been examined through simulated comparisons under different HONO concentrations (Fig. S8). The observed and modeled O_3 concentrations in Fig. 8d are averaged for the daytime period between 10:00 and 15:00 CST. The observed diurnal ozone concentrations were 75.7 and 78.6 ppb during the LAM and OCM periods, respectively. The daytime ozone was well reproduced by the time-dependent box model, and the deviation of the simulation was less than 20 % (Fig. 8d). After removing the HONO constraint, the simulated ozone concentrations were 38.2 and 26.3 ppb, i.e., 48 % and 58 % lower, during the LAM and OCM periods, respectively. Simulated O_3 decreased from ~ 75 ppb to a global background concentration, and daytime HONO concentrations were reduced to a low level (~ 70 ppt) (Woodward-Massey et al., 2023; Zhu et al., 2022; Xia et al., 2022). The elevated daytime HONO had an additional effect on oxidation in the background atmosphere. For coastal cities, the particularity of the HONO chemistry in the MBL tends to influence the ozone-sensitive system and eventually magnifies the background ozone. Therefore, the promotion of oxidation by elevated precursor concentrations is worth considering when formulating emission reduction policies. In regions where HONO concentrations are elevated, the sources of HONO would need to be identified to aid pollution mitigation policies.

5 Conclusions

Comprehensive observations of HO_x radicals and other relevant species were conducted in October 2019 at a coastal site in the Pearl River Delta (the YMK site, 22.55° N, 114.60° E). The overall air pollutants exhibited typical coastal features owing to the scarce anthropogenic emissions. The daily maximum OH and HO_2 concentrations were (4.7–9.5) × 10^6 and (4.2–8.1) × 10^8 cm^{-3}, respectively. The base RACM2-LIM1 model satisfactorily reproduced the observed OH and HO_2 radical concentrations, but a slight overestimation of the OH radical occurred. The daily maximum calculated total OH re-

activity was $9.9\,s^{-1}$, and nearly 70 % of the reactivity was contributed by organic species.

In addition to anthropogenic and vegetation emissions, the synchronized air mass transport from the northern cities and the South China Sea exerted a time-varying influence on radical photochemistry and atmospheric oxidation. During the OCM period, the observed OH and HO_2 radical concentrations could be reflected by the base chemical mechanism, with daily average values of 4.5×10^6 and $4.9 \times 10^8\,cm^{-3}$, respectively.

In the episode that was dominated by ocean mass, the $HO_2 + NO$ reaction accounted for ~ 50 % of the primary OH yield. A higher OH generation rate was found ($12.6\,ppb\,h^{-1}$) during the LAM period, and the secondary source accounted for 67 % of the total, which was similar to several observations in polluted plumes. Reactions between RO_x and NO_x and self-combination were the main pathways of radical termination (~ 70 %), and the contribution of peroxynitrate formation to the $L(RO_x)$ could not be ignored during the daytime.

Intensive photochemical reactions occur after the accumulation of precursors, resulting in local net ozone production comparable with that in the surrounding suburban environments. The daily average ozone production rates were 5.52 and $2.76\,ppb\,h^{-1}$ during the LAM and OCM periods, respectively. The rapid oxidation process was accompanied by a higher diurnal HONO concentration (higher than 400 ppt). A non-HONO-constrained sensitivity test was performed to quantify the HONO-induced contribution to secondary pollution. After evaluation, the $P(O_x)$ values were 33 % and 39 % lower during the LAM and OCM periods, respectively. The nitric acid ($P(HNO_3)$) and sulfuric acid ($P(H_2SO_4)$) formation rates also increased simultaneously (~ 43 % and ~ 48 % for the LAM and OCM sectors, respectively). Simulated O_3 decreased from ~ 75 ppb to a global background, and daytime HONO concentrations were reduced to a low level (~ 70 ppt). For coastal cities, the particularity of the HONO chemistry in the MBL tends to influence the ozone-sensitive system and eventually magnifies the background ozone. Therefore, the promotion of oxidation by elevated precursor concentrations is worth considering when formulating emission reduction policies.

Data availability. The data used in this study are available from the corresponding author upon request (rzhu@aiofm.ac.cn).

Supplement. The supplement related to this article is available online at: https://doi.org/10.5194/acp-24-1825-2024-supplement.

Author contributions. WL, PX, RH contributed to the conception of this study. GZ and RH performed the data analyses and manuscript writing. All authors contributed to measurements, discussed results, and commented on the paper.

Competing interests. The contact author has declared that none of the authors has any competing interests.

Disclaimer. Publisher's note: Copernicus Publications remains neutral with regard to jurisdictional claims made in the text, published maps, institutional affiliations, or any other geographical representation in this paper. While Copernicus Publications makes every effort to include appropriate place names, the final responsibility lies with the authors.

Acknowledgements. The authors appreciate the valuable comments from two anonymous reviewers.

Financial support. This research has been supported by the National Natural Science Foundation of China (grant nos. 62275250, U19A2044, and 61905003), the Natural Science Foundation of Anhui Province (grant no. 2008085J20), the National Key Research and Development Program of China (grant no. 2022YFC3700301), the Anhui Provincial Key Research and Development Plan (grant no. 2022l07020022), and the Beijing Municipal Natural Science Fund for Distinguished Young Scholars (grant no. JQ21030).

Review statement. This paper was edited by Yugo Kanaya and reviewed by two anonymous referees.

References

Bloss, W. J., Camredon, M., Lee, J. D., Heard, D. E., Plane, J. M. C., Saiz-Lopez, A., Bauguitte, S. J.-B., Salmon, R. A., and Jones, A. E.: Coupling of HO_x, NO_x and halogen chemistry in the antarctic boundary layer, Atmos. Chem. Phys., 10, 10187–10209, https://doi.org/10.5194/acp-10-10187-2010, 2010.

Brauers, T., Hausmann, M., Bister, A., Kraus, A., and Dorn, H.-P.: OH radicals in the boundary layer of the Atlantic Ocean: 1. Measurements by long-path laser absorption spectroscopy, J. Geophys. Res., 106, 7399, https://doi.org/10.1029/2000jd900679, 2001.

Carpenter, L. J., Fleming, Z. L., Read, K. A., Lee, J. D., Moller, S. J., Hopkins, J. R., Purvis, R. M., Lewis, A. C., Müller, K., Heinold, B., Herrmann, H., Fomba, K. W., van Pinxteren, D., Müller, C., Tegen, I., Wiedensohler, A., Müller, T., Niedermeier, N., Achterberg, E. P., Patey, M. D., Kozlova, E. A., Heimann, M., Heard, D. E., Plane, J. M. C., Mahajan, A., Oetjen, H., Ingham, T., Stone, D., Whalley, L. K., Evans, M. J., Pilling, M. J., Leigh, R. J., Monks, P. S., Karunaharan, A., Vaughan, S., Arnold, S. R., Tschritter, J., Pöhler, D., Frieß, U., Holla, R., Mendes, L. M., Lopez, H., Faria, B., Manning, A. J., and Wallace, D. W. R.: Seasonal characteristics of tropical marine boundary layer air measured at the Cape Verde Atmospheric Observatory, J. Atmos.

Chem., 67, 87–140, https://doi.org/10.1007/s10874-011-9206-1, 2011.

Carslaw, N., Creasey, D. J., Heard, D. E., Lewis, A. C., McQuaid, J. B., Pilling, M. J., Monks, P. S., Bandy, B. J., and Penkett, S. A.: Modeling OH, HO_2, and RO_2 radicals in the marine boundary layer: 1. Model construction and comparison with field measurements, J. Geophys. Res.-Atmos., 104, 30241–30255, https://doi.org/10.1029/1999jd900783, 1999.

Chen, W., Guenther, A. B., Shao, M., Yuan, B., Jia, S., Mao, J., Yan, F., Krishnan, P., and Wang, X.: Assessment of background ozone concentrations in China and implications for using region-specific volatile organic compounds emission abatement to mitigate air pollution, Environ. Pollut., 305, 119254, https://doi.org/10.1016/j.envpol.2022.119254, 2022.

Creasey, D. J., Heard, D. E., and Lee, J. D.: Eastern Atlantic Spring Experiment 1997 (EASE97) 1. Measurements of OH and HO_2concentrations at Mace Head, Ireland, J. Geophys. Res.-Atmos., 107, ACH 3-1–ACH 3-15, https://doi.org/10.1029/2001jd000892, 2002.

Crilley, L. R., Kramer, L. J., Pope, F. D., Reed, C., Lee, J. D., Carpenter, L. J., Hollis, L. D. J., Ball, S. M., and Bloss, W. J.: Is the ocean surface a source of nitrous acid (HONO) in the marine boundary layer?, Atmos. Chem. Phys., 21, 18213–18225, https://doi.org/10.5194/acp-21-18213-2021, 2021.

Fuchs, H., Dorn, H.-P., Bachner, M., Bohn, B., Brauers, T., Gomm, S., Hofzumahaus, A., Holland, F., Nehr, S., Rohrer, F., Tillmann, R., and Wahner, A.: Comparison of OH concentration measurements by DOAS and LIF during SAPHIR chamber experiments at high OH reactivity and low NO concentration, Atmos. Meas. Tech., 5, 1611–1626, https://doi.org/10.5194/amt-5-1611-2012, 2012.

Fuchs, H., Tan, Z., Lu, K., Bohn, B., Broch, S., Brown, S. S., Dong, H., Gomm, S., Häseler, R., He, L., Hofzumahaus, A., Holland, F., Li, X., Liu, Y., Lu, S., Min, K.-E., Rohrer, F., Shao, M., Wang, B., Wang, M., Wu, Y., Zeng, L., Zhang, Y., Wahner, A., and Zhang, Y.: OH reactivity at a rural site (Wangdu) in the North China Plain: contributions from OH reactants and experimental OH budget, Atmos. Chem. Phys., 17, 645–661, https://doi.org/10.5194/acp-17-645-2017, 2017.

Grenfell, J. L., Savage, N. H., Harrison, R. M., Penkett, S. A., Forberich, O., Comes, F. J., Clemitshaw, K. C., Burgess, R. A., Cardenas, L. M., Davison, B., and McFadyen, G. G.: Tropospheric box-modelling and analytical studies of the hydroxyl (OH) radical and related species: Comparison with observations, J. Atmos. Chem., 33, 183–214, https://doi.org/10.1023/a:1006009901180, 1999.

Griffith, S. M., Hansen, R. F., Dusanter, S., Stevens, P. S., Alaghmand, M., Bertman, S. B., Carroll, M. A., Erickson, M., Galloway, M., Grossberg, N., Hottle, J., Hou, J., Jobson, B. T., Kammrath, A., Keutsch, F. N., Lefer, B. L., Mielke, L. H., O'Brien, A., Shepson, P. B., Thurlow, M., Wallace, W., Zhang, N., and Zhou, X. L.: OH and HO_2 radical chemistry during PROPHET 2008 and CABINEX 2009 – Part 1: Measurements and model comparison, Atmos. Chem. Phys., 13, 5403–5423, https://doi.org/10.5194/acp-13-5403-2013, 2013.

Huang, R. J., Hoffmann, T., Ovadnevaite, J., Laaksonen, A., Kokkola, H., Xu, W., Xu, W., Ceburnis, D., Zhang, R., Seinfeld, J. H., and O'Dowd, C.: Heterogeneous iodine-organic chemistry fast-tracks marine new particle formation, P. Natl. Acad. Sci. USA, 119, e2201729119, https://doi.org/10.1073/pnas.2201729119, 2022.

Jiang, Y., Xue, L., Shen, H., Dong, C., Xiao, Z., and Wang, W.: Dominant Processes of HONO Derived from Multiple Field Observations in Contrasting Environments, Environ. Sci. Technol. Lett., 9, 258–264, https://doi.org/10.1021/acs.estlett.2c00004, 2022.

Kanaya, Y., Sadanaga, Y., Nakamura, K., and Akimoto, H.: Behavior of OH and HO_2 radicals during the Observations at a Remote Island of Okinawa (ORION99) field campaign 1. Observation using a laser-induced fluorescence instrument, J. Geophys. Res.-Atmos., 106, 24197–24208, https://doi.org/10.1029/2000jd000178, 2001.

Kanaya, Y., Yokouchi, Y., Matsumoto, J., Nakamura, K., Kato, S., Tanimoto, H., Furutani, H., Toyota, K., and Akimoto, H.: Implications of iodine chemistry for daytime HO_2levels at Rishiri Island, Geophys. Res. Lett., 29, 45-41–45-44, https://doi.org/10.1029/2001gl014061, 2002.

Liu, C., Liu, G., Casazza, M., Yan, N., Xu, L., Hao, Y., Franzese, P. P., and Yang, Z.: Current Status and Potential Assessment of China's Ocean Carbon Sinks, Environ. Sci. Technol., 56, 6584–6595, https://doi.org/10.1021/acs.est.1c08106, 2022.

Liu, P., Xue, C., Ye, C., Liu, C., Zhang, C., Wang, J., Zhang, Y., Liu, J., and Mu, Y.: The Lack of HONO Measurement May Affect the Accurate Diagnosis of Ozone Production Sensitivity, ACS Environmental Au, 3, 18–23, https://doi.org/10.1021/acsenvironau.2c00048, 2022.

Liu, T., Hong, Y., Li, M., Xu, L., Chen, J., Bian, Y., Yang, C., Dan, Y., Zhang, Y., Xue, L., Zhao, M., Huang, Z., and Wang, H.: Atmospheric oxidation capacity and ozone pollution mechanism in a coastal city of southeastern China: analysis of a typical photochemical episode by an observation-based model, Atmos. Chem. Phys., 22, 2173–2190, https://doi.org/10.5194/acp-22-2173-2022, 2022.

Lou, S., Holland, F., Rohrer, F., Lu, K., Bohn, B., Brauers, T., Chang, C. C., Fuchs, H., Häseler, R., Kita, K., Kondo, Y., Li, X., Shao, M., Zeng, L., Wahner, A., Zhang, Y., Wang, W., and Hofzumahaus, A.: Atmospheric OH reactivities in the Pearl River Delta – China in summer 2006: measurement and model results, Atmos. Chem. Phys., 10, 11243–11260, https://doi.org/10.5194/acp-10-11243-2010, 2010.

Lu, K. D., Rohrer, F., Holland, F., Fuchs, H., Bohn, B., Brauers, T., Chang, C. C., Häseler, R., Hu, M., Kita, K., Kondo, Y., Li, X., Lou, S. R., Nehr, S., Shao, M., Zeng, L. M., Wahner, A., Zhang, Y. H., and Hofzumahaus, A.: Observation and modelling of OH and HO_2 concentrations in the Pearl River Delta 2006: a missing OH source in a VOC rich atmosphere, Atmos. Chem. Phys., 12, 1541–1569, https://doi.org/10.5194/acp-12-1541-2012, 2012.

Lu, K. D., Hofzumahaus, A., Holland, F., Bohn, B., Brauers, T., Fuchs, H., Hu, M., Häseler, R., Kita, K., Kondo, Y., Li, X., Lou, S. R., Oebel, A., Shao, M., Zeng, L. M., Wahner, A., Zhu, T., Zhang, Y. H., and Rohrer, F.: Missing OH source in a suburban environment near Beijing: observed and modelled OH and HO_2 concentrations in summer 2006, Atmos. Chem. Phys., 13, 1057–1080, https://doi.org/10.5194/acp-13-1057-2013, 2013.

Lu, K. D., Guo, S., Tan, Z. F., Wang, H. C., Shang, D. J., Liu, Y. H., Li, X., Wu, Z. J., Hu, M., and Zhang, Y. H.: Exploring atmospheric free-radical chemistry in China: the self-cleansing capac-

ity and the formation of secondary air pollution, Natl. Sci. Rev., 6, 579–594, https://doi.org/10.1093/nsr/nwy073, 2019.

Ma, X. F., Tan, Z. F., Lu, K. D., Yang, X. P., Liu, Y. H., Li, S. L., Li, X., Chen, S. Y., Novelli, A., Cho, C. M., Zeng, L. M., Wahner, A., and Zhang, Y. H.: Winter photochemistry in Beijing: Observation and model simulation of OH and HO_2 radicals at an urban site, Sci. Total Environ., 685, 85–95, https://doi.org/10.1016/j.scitotenv.2019.05.329, 2019.

Mallik, C., Tomsche, L., Bourtsoukidis, E., Crowley, J. N., Derstroff, B., Fischer, H., Hafermann, S., Hüser, I., Javed, U., Keßel, S., Lelieveld, J., Martinez, M., Meusel, H., Novelli, A., Phillips, G. J., Pozzer, A., Reiffs, A., Sander, R., Taraborrelli, D., Sauvage, C., Schuladen, J., Su, H., Williams, J., and Harder, H.: Oxidation processes in the eastern Mediterranean atmosphere: evidence from the modelling of HO_x measurements over Cyprus, Atmos. Chem. Phys., 18, 10825–10847, https://doi.org/10.5194/acp-18-10825-2018, 2018.

Niu, Y. B., Zhu, B., He, L. Y., Wang, Z., Lin, X. Y., Tang, M. X., and Huang, X. F.: Fast Nocturnal Heterogeneous Chemistry in a Coastal Background Atmosphere and Its Implications for Daytime Photochemistry, J. Geophys. Res.-Atmos., 127, e2022JD036716, https://doi.org/10.1029/2022jd036716, 2022.

Peng, X., Wang, W. H., Xia, M., Chen, H., Ravishankara, A. R., Li, Q. Y., Saiz-Lopez, A., Liu, P. F., Zhang, F., Zhang, C. L., Xue, L. K., Wang, X. F., George, C., Wang, J. H., Mu, Y. J., Chen, J. M., and Wang, T.: An unexpected large continental source of reactive bromine and chlorine with significant impact on wintertime air quality, Natl. Sci. Rev., 8, nwaa304, https://doi.org/10.1093/nsr/nwaa304, 2021.

Qi, B., Kanaya, Y., Takami, A., Hatakeyama, S., Kato, S., Sadanaga, Y., Tanimoto, H., and Kajii, Y.: Diurnal peroxy radical chemistry at a remote coastal site over the sea of Japan, J. Geophys. Res., 112, D17306, https://doi.org/10.1029/2006jd008236, 2007.

Slater, E. J., Whalley, L. K., Woodward-Massey, R., Ye, C., Lee, J. D., Squires, F., Hopkins, J. R., Dunmore, R. E., Shaw, M., Hamilton, J. F., Lewis, A. C., Crilley, L. R., Kramer, L., Bloss, W., Vu, T., Sun, Y., Xu, W., Yue, S., Ren, L., Acton, W. J. F., Hewitt, C. N., Wang, X., Fu, P., and Heard, D. E.: Elevated levels of OH observed in haze events during wintertime in central Beijing, Atmos. Chem. Phys., 20, 14847–14871, https://doi.org/10.5194/acp-20-14847-2020, 2020.

Song, H., Lu, K., Dong, H., Tan, Z., Chen, S., Zeng, L., and Zhang, Y.: Reduced Aerosol Uptake of Hydroperoxyl Radical May Increase the Sensitivity of Ozone Production to Volatile Organic Compounds, Environ. Sci. Technol. Lett., 9, 22–29, https://doi.org/10.1021/acs.estlett.1c00893, 2021.

Stockwell, W. R., Kirchner, F., Kuhn, M., and Seefeld, S.: A new mechanism for regional atmospheric chemistry modeling, J. Geophys. Res.-Atmos., 102, 25847–25879, https://doi.org/10.1029/97jd00849, 1997.

Stone, D., Whalley, L. K., and Heard, D. E.: Tropospheric OH and HO_2 radicals: field measurements and model comparisons, Chem. Soc. Rev., 41, 6348–6404, https://doi.org/10.1039/c2cs35140d, 2012.

Sun, L., Chen, T., Jiang, Y., Zhou, Y., Sheng, L., Lin, J., Li, J., Dong, C., Wang, C., Wang, X., Zhang, Q., Wang, W., and Xue, L.: Ship emission of nitrous acid (HONO) and its impacts on the marine atmospheric oxidation chemistry, Sci. Total Environ., 735, 139355, https://doi.org/10.1016/j.scitotenv.2020.139355, 2020.

Tan, Z., Fuchs, H., Lu, K., Hofzumahaus, A., Bohn, B., Broch, S., Dong, H., Gomm, S., Häseler, R., He, L., Holland, F., Li, X., Liu, Y., Lu, S., Rohrer, F., Shao, M., Wang, B., Wang, M., Wu, Y., Zeng, L., Zhang, Y., Wahner, A., and Zhang, Y.: Radical chemistry at a rural site (Wangdu) in the North China Plain: observation and model calculations of OH, HO_2 and RO_2 radicals, Atmos. Chem. Phys., 17, 663–690, https://doi.org/10.5194/acp-17-663-2017, 2017.

Tan, Z., Lu, K., Jiang, M., Su, R., Wang, H., Lou, S., Fu, Q., Zhai, C., Tan, Q., Yue, D., Chen, D., Wang, Z., Xie, S., Zeng, L., and Zhang, Y.: Daytime atmospheric oxidation capacity in four Chinese megacities during the photochemically polluted season: a case study based on box model simulation, Atmos. Chem. Phys., 19, 3493–3513, https://doi.org/10.5194/acp-19-3493-2019, 2019a.

Tan, Z., Lu, K., Hofzumahaus, A., Fuchs, H., Bohn, B., Holland, F., Liu, Y., Rohrer, F., Shao, M., Sun, K., Wu, Y., Zeng, L., Zhang, Y., Zou, Q., Kiendler-Scharr, A., Wahner, A., and Zhang, Y.: Experimental budgets of OH, HO_2, and RO_2 radicals and implications for ozone formation in the Pearl River Delta in China 2014, Atmos. Chem. Phys., 19, 7129–7150, https://doi.org/10.5194/acp-19-7129-2019, 2019b.

Tan, Z., Lu, K., Ma, X., Chen, S., He, L., Huang, X., Li, X., Lin, X., Tang, M., Yu, D., Wahner, A., and Zhang, Y.: Multiple Impacts of Aerosols on O(3) Production Are Largely Compensated: A Case Study Shenzhen, China, Environ. Sci. Technol., 56, 17569–17580, https://doi.org/10.1021/acs.est.2c06217, 2022.

Tan, Z. F., Lu, K. D., Jiang, M. Q., Su, R., Dong, H. B., Zeng, L. M., Xie, S. D., Tan, Q. W., and Zhang, Y. H.: Exploring ozone pollution in Chengdu, southwestern China: A case study from radical chemistry to O3-VOC-NO_x sensitivity, Sci. Total Environ., 636, 775–786, https://doi.org/10.1016/j.scitotenv.2018.04.286, 2018a.

Tan, Z. F., Lu, K. D., Dong, H. B., Hu, M., Li, X., Liu, Y. H., Lu, S. H., Shao, M., Su, R., Wang, H. C., Wu, Y. S., Wahner, A., and Zhang, Y. H.: Explicit diagnosis of the local ozone production rate and the ozone-NO_x-VOC sensitivities, Sci. Bull., 63, 1067–1076, https://doi.org/10.1016/j.scib.2018.07.001, 2018b.

Vaughan, S., Ingham, T., Whalley, L. K., Stone, D., Evans, M. J., Read, K. A., Lee, J. D., Moller, S. J., Carpenter, L. J., Lewis, A. C., Fleming, Z. L., and Heard, D. E.: Seasonal observations of OH and HO_2 in the remote tropical marine boundary layer, Atmos. Chem. Phys., 12, 2149–2172, https://doi.org/10.5194/acp-12-2149-2012, 2012.

Wang, F., Hu, R., Xie, P., Wang, Y., Chen, H., Zhang, G., and Liu, W.: Calibration source for OH radical based on synchronous photolysis, Acta Phys. Sin.-Ch. Ed., 69, 090701, https://doi.org/10.7498/aps.69.20200153, 2020.

Wang, F. Y., Hu, R. Z., Chen, H., Xie, P. H., Wang, Y. H., Li, Z. Y., Jin, H. W., Liu, J. G., and Liu, W. Q.: Development of a field system for measurement of tropospheric OH radical using laser-induced fluorescence technique, Opt. Express, 27, A419–A435, https://doi.org/10.1364/oe.27.00a419, 2019.

Wang, J., Zhang, Y., Zhang, C., Wang, Y., Zhou, J., Whalley, L. K., Slater, E. J., Dyson, J. E., Xu, W., Cheng, P., Han, B., Wang, L., Yu, X., Wang, Y., Woodward-Massey, R., Lin, W., Zhao, W., Zeng, L., Ma, Z., Heard, D. E., and Ye, C.: Validating HONO as an Intermediate Tracer of the External Cycling of Reactive

Nitrogen in the Background Atmosphere, Environ. Sci. Technol., 57, 5474–5484, https://doi.org/10.1021/acs.est.2c06731, 2023.

Wang, T., Wei, X. L., Ding, A. J., Poon, C. N., Lam, K. S., Li, Y. S., Chan, L. Y., and Anson, M.: Increasing surface ozone concentrations in the background atmosphere of Southern China, 1994–2007, Atmos. Chem. Phys., 9, 6217–6227, https://doi.org/10.5194/acp-9-6217-2009, 2009.

Wang, Y., Hu, R., Xie, P., Chen, H., Wang, F., Liu, X., Liu, J., and Liu, W.: Measurement of tropospheric HO_2 radical using fluorescence assay by gas expansion with low interferences, J. Environ. Sci. (China), 99, 40–50, https://doi.org/10.1016/j.jes.2020.06.010, 2021.

Whalley, L. K., Furneaux, K. L., Goddard, A., Lee, J. D., Mahajan, A., Oetjen, H., Read, K. A., Kaaden, N., Carpenter, L. J., Lewis, A. C., Plane, J. M. C., Saltzman, E. S., Wiedensohler, A., and Heard, D. E.: The chemistry of OH and HO2 radicals in the boundary layer over the tropical Atlantic Ocean, Atmos. Chem. Phys., 10, 1555–1576, https://doi.org/10.5194/acp-10-1555-2010, 2010.

Woodward-Massey, R., Sommariva, R., Whalley, L. K., Cryer, D. R., Ingham, T., Bloss, W. J., Ball, S. M., Cox, S., Lee, J. D., Reed, C. P., Crilley, L. R., Kramer, L. J., Bandy, B. J., Forster, G. L., Reeves, C. E., Monks, P. S., and Heard, D. E.: Radical chemistry and ozone production at a UK coastal receptor site, Atmos. Chem. Phys., 23, 14393–14424, https://doi.org/10.5194/acp-23-14393-2023, 2023.

Xia, M., Wang, T., Wang, Z., Chen, Y., Peng, X., Huo, Y., Wang, W., Yuan, Q., Jiang, Y., Guo, H., Lau, C., Leung, K., Yu, A., and Lee, S.: Pollution-Derived Br_2 Boosts Oxidation Power of the Coastal Atmosphere, Environ. Sci. Technol., 56, 11909–12784, https://doi.org/10.1021/acs.est.2c02434, 2022.

Xia, S.-Y., Zhu, B., Wang, S.-X., Huang, X.-F., and He, L.-Y.: Spatial distribution and source apportionment of peroxyacetyl nitrate (PAN) in a coastal region in southern China, Atmos. Environ., 260, 118553, https://doi.org/10.1016/j.atmosenv.2021.118553, 2021.

Xu, W., Ovadnevaite, J., Fossum, K. N., Lin, C., Huang, R.-J., Ceburnis, D., and O'Dowd, C.: Sea spray as an obscured source for marine cloud nuclei, Nat. Geosci., 15, 282–286, https://doi.org/10.1038/s41561-022-00917-2, 2022.

Yang, X., Lu, K., Ma, X., Liu, Y., Wang, H., Hu, R., Li, X., Lou, S., Chen, S., Dong, H., Wang, F., Wang, Y., Zhang, G., Li, S., Yang, S., Yang, Y., Kuang, C., Tan, Z., Chen, X., Qiu, P., Zeng, L., Xie, P., and Zhang, Y.: Observations and modeling of OH and HO_2 radicals in Chengdu, China in summer 2019, Sci. Total Environ., 772, 144829–144829, https://doi.org/10.1016/j.scitotenv.2020.144829, 2021a.

Yang, Y., Li, X., Zu, K., Lian, C., Chen, S., Dong, H., Feng, M., Liu, H., Liu, J., Lu, K., Lu, S., Ma, X., Song, D., Wang, W., Yang, S., Yang, X., Yu, X., Zhu, Y., Zeng, L., Tan, Q., and Zhang, Y.: Elucidating the effect of HONO on O_3 pollution by a case study in southwest China, Sci. Total Environ., 756, 144127, https://doi.org/10.1016/j.scitotenv.2020.144127, 2021b.

Yang, X., Lu, K., Ma, X., Gao, Y., Tan, Z., Wang, H., Chen, X., Li, X., Huang, X., He, L., Tang, M., Zhu, B., Chen, S., Dong, H., Zeng, L., and Zhang, Y.: Radical chemistry in the Pearl River Delta: observations and modeling of OH and HO_2 radicals in Shenzhen in 2018, Atmos. Chem. Phys., 22, 12525–12542, https://doi.org/10.5194/acp-22-12525-2022, 2022.

Zeren, Y., Zhou, B., Zheng, Y., Jiang, F., Lyu, X., Xue, L., Wang, H., Liu, X., and Guo, H.: Does Ozone Pollution Share the Same Formation Mechanisms in the Bay Areas of China?, Environ. Sci. Technol., 56, 14326–14337, https://doi.org/10.1021/acs.est.2c05126, 2022.

Zhang, G., Hu, R., Xie, P., Lou, S., Wang, F., Wang, Y., Qin, M., Li, X., Liu, X., Wang, Y., and Liu, W.: Observation and simulation of HO_x radicals in an urban area in Shanghai, China, Sci. Total Environ., 810, 152275, https://doi.org/10.1016/j.scitotenv.2021.152275, 2022a.

Zhang, G., Hu, R., Xie, P., Lu, K., Lou, S., Liu, X., Li, X., Wang, F., Wang, Y., Yang, X., Cai, H., Wang, Y., and Liu, W.: Intercomparison of OH radical measurement in a complex atmosphere in Chengdu, China, Sci. Total Environ., 838, 155924, https://doi.org/10.1016/j.scitotenv.2022.155924, 2022b.

Zhu, B., Huang, X.-F., Xia, S.-Y., Lin, L.-L., Cheng, Y., and He, L.-Y.: Biomass-burning emissions could significantly enhance the atmospheric oxidizing capacity in continental air pollution, Environ. Pollut., 285, 117523, https://doi.org/10.1016/j.envpol.2021.117523, 2021.

Zhu, Y., Wang, Y., Zhou, X., Elshorbany, Y. F., Ye, C., Hayden, M., and Peters, A. J.: An investigation into the chemistry of HONO in the marine boundary layer at Tudor Hill Marine Atmospheric Observatory in Bermuda, Atmos. Chem. Phys., 22, 6327–6346, https://doi.org/10.5194/acp-22-6327-2022, 2022.

Zou, Z., Chen, Q., Xia, M., Yuan, Q., Chen, Y., Wang, Y., Xiong, E., Wang, Z., and Wang, T.: OH measurements in the coastal atmosphere of South China: possible missing OH sinks in aged air masses, Atmos. Chem. Phys., 23, 7057–7074, https://doi.org/10.5194/acp-23-7057-2023, 2023.